

Algorithms for autonomous exploration and estimation in compliant environments

R. E. Goldman[†], A. Bajo[‡] and N. Simaan^{‡*}

[†]Department of Biomedical Engineering, Columbia University, New York, NY 10027 USA

[‡]Department of Mechanical Engineering, Vanderbilt University, Nashville, TN 37235 USA

(Accepted February 20, 2011)

SUMMARY

This paper investigates algorithms for enabling surgical slave robots to autonomously explore shape and stiffness of surgical fields. The paper addresses methods for estimating shape and impedance parameters of tissue and methods for autonomously exploring perceived impedance during tool interaction inside a tissue cleft. A hybrid force-motion controller and a cycloidal motion path are proposed to address shape exploration. An adaptive exploration algorithm for segmentation of surface features and a predictor-corrector algorithm for exploration of deep features are introduced based on discrete impedance estimates. These estimates are derived from localized excitation of tissue coupled with simultaneous force measurements. Shape estimation is validated in *ex-vivo* bovine tissue and attains surface estimation errors of less than 2.5 mm with force sensing resolutions achievable with current technologies in minimally invasive surgical robots. The effect of scan patterns on the accuracy of the shape estimate is demonstrated by comparing the shape estimate of a Cartesian raster scan with overlapping cycloid scan pattern. It is shown that the latter pattern filters the shape estimation bias due to frictional drag forces. Surface impedance exploration is validated to successfully segment compliant environments on flexible inorganic models. Simulations and experiments show that the adaptive search algorithm reduces overall time requirements relative to the complexity of the underlying structures. Finally, autonomous exploration of deep features is demonstrated in an inorganic model and *ex-vivo* bovine tissue. It is shown that estimates of least constraint based on singular value decomposition of locally estimated tissue stiffness can generate motion to accurately follow a tissue cleft with a predictor-corrector algorithm employing alternating steps of position and admittance control. We believe that these results demonstrate the potential of these algorithms for enabling “smart” surgical devices capable of autonomous execution of intraoperative surgical plans.

KEYWORDS: Autonomous exploration; Environment impedance estimation; Hybrid force-motion control; Computer-assisted surgery.

* Corresponding author. E-mail: nabil.simaan@vanderbilt.edu
This research has been partly supported by NSF Career grant IIS#1063750.

1. Introduction

Integration of preoperative geometric data into the surgical work flow by robotic and computer-assisted surgical systems produced a disruptive technology allowing significant improvement in the treatment of disease through minimally invasive surgery (MIS) techniques. Examples in radiosurgery, stereotactic neurosurgery, otolaryngologic surgery, and orthopedic surgery demonstrate the use of preoperative data sets to augment the surgical system in modalities requiring precision and navigation beyond manual human abilities.⁴⁴ With few exceptions, data integration relies on rigid anatomic landmarks or exogenous fiducials. The utility of the preoperative imaging studies for directing intraoperative behavior is severely limited by anatomic changes in the surgical environment created by patient positioning and clinical intervention. This limitation precludes the use of assistive technologies, such as active constraint control or virtual fixtures^{1,21,25} or passive navigation assistance, for the improvement of MIS on deformable tissue structures since an accurate model of the immediate environment is unavailable or substantially deviated from preoperative imaging data. Methods for acquisition and intelligent use of real-time intraoperative sensory information to augment preoperative data, we believe, will result in a new generation of “smart” surgical robots that apply control updates to augment the system function based on measured environmental clues.^{10,44}

Intelligent use of on-line data by “smart” surgical robots will enable surgeons to make strides in the complexity of techniques, precision, and overall capabilities of surgical procedures. These improvements will be made by adapting to the environment during teleoperation in order to make surgical slaves behave more reliably or safely. Improved intraoperative data integration will also allow autonomous performance of low level tasks by a surgical slave. An initial requirement to facilitate this interaction is online acquisition of environment data and formulation of digital models for actionable control laws.

Sensing modalities for acquiring environment data during MIS are used sparsely during robotic procedures due to the complexity of both obtaining reliable data and applying this data intraoperatively in a method useful to the operator. Sole reliance on imaging data for surgical execution presents a significant limitation of current robotic systems. Intraoperative imaging can be constrained either by environmental conditions or clinical considerations.

An example of the former is the inability to use light-based imaging during intravascular procedures where blood obfuscates the image. An example of the latter is the desire to limit exposure to radiation or the undesirable space and compatibility constraints imposed by intraoperative MRI.

Mechanical environment exploration can augment and enhance imaging modalities. In the setting of open surgery, surgeons are able to perform blind exploration to characterize tissue. They can determine the shape and stiffness of organs through palpation and manipulation and can insert their fingers in crevices or behind organs to identify invisible structures while moving safely along natural separation boundaries between neighboring structures. In robotic MIS, mechanical exploration can extend and patch image-based surface environment models by exploring areas hidden to the camera. Additionally, mechanical exploration can add a dimension to the intraoperative digital model by including information on the tissue characteristics such as stiffness. Finally, in scenarios where a surgical instrument is maneuvered along the separation plane of connective tissue between organs, mechanical exploration can provide useful information for autonomous motion and for constructing assistive telemanipulation virtual fixtures. Current robotic systems lack these capabilities, partly due to deficient sensing modalities, but mostly due to a lack of algorithms to guide exploration in flexible unstructured environments such as MIS surgical fields.

In this work, we propose algorithms for autonomous exploration of the shape and the mechanical impedance parameters of an unknown flexible environment using only force and position information. We believe, acquisition of this data provides an essential missing element to augment or replace preoperatively generated models and simultaneously enhance intraoperative imaging modalities. Furthermore, an autonomous approach allows the control architecture to change from passive telemanipulation control to operator-initiated autonomous exploration. This technology will allow surgical slaves to collect information without direct telemanipulation control from a remote operator; thus, allowing the operator to focus on higher-level, more demanding intraoperative tasks.

2. Background, Research Approach and Contribution

2.1. Works on exploration, mechanical probing and imaging

The proposed algorithms, taken together, represent an extension of previous research in shape, impedance, and constraint estimation toward exploration in the setting of robotic MIS. The combined literature forms a basis for the proposed works and highlights the need for suitable algorithms for exploration in compliant environments.

Shape models are critical for integration of intelligence into robotic surgical systems and a fundamental component to be developed for this purpose. Vision systems are an obvious first step for this purpose due to the time cost relative to the coverage but will not form complete models where the image is obscured. Exploratory procedures have therefore been proposed to supplement visual modalities

using a combination of tactile sensing, force sensing, and proprioception for rigid objects and environments. Allen and Michelman⁴ proposed and investigated different mappings for intelligent shape recognition from tactile sensing for surface regions of rigid objects. Okamura and Cutkosky³⁶ investigated strategies for exploration of rigid environments and surface feature detection, such as cracks or ridges, using robotic fingers equipped with tactile sensors. Moll and Erdmann³⁴ proposed algorithms for shape reconstruction of planar objects rolled between two hands equipped with tactile sensors. Multiple groups,^{2,6,18,22,50} have proposed algorithms for contour tracking of surfaces using impedance or force-motion control algorithms. The majority of these works focused on cases of rigid or structured environments and thus the methods require adaption for MIS where the exploration site is highly unstructured and variably compliant. Doulgeri and Karayiannidis¹³ propose a control law for regulation of force and position with an unknown compliant surface. The method relies on joint level torque estimates for estimating the disturbance and confirmed the results under relatively stiff environments. Our particular experience with soft media, such as tissue, has shown that the signal to noise ratio limits the ability to estimate position and the surface normal simultaneously as will be elaborated.

During interaction with geometrically complex environments, shape exploration must be augmented to include the interaction of the instrument tool with the environment to model constraints opposing motion. Yoshikawa *et al.*⁵¹ proposed a method for estimation of polyhedral contact constraints using exploratory probing operations. Eberman¹⁴ proposed a maximum likelihood estimator for contact state in a planar Cartesian system. Debus *et al.*¹¹ applied a hidden Markov model to identify predefined geometric constraints using kinematic sensors. Lefebvre *et al.*²⁹ used stochastic estimation to identify rigid, frictionless contact constraints. As above, the relevant works highlight methods for rigid, and generally structured, environments common to industrial processes for which robots have been primarily deployed. Robotic MIS surgery requires methods for understanding instrument contact constraints during complex interaction such as dissection, suturing, and tissue manipulation.

Palpation, a common modality of exploration in the context of surgical care, has been widely studied for restoration in robotic systems. The research community has focused on palpation and segmentation of embedded structures in flexible media such as tissue. Sabatini *et al.*³⁹ investigated models of interaction between an instrumented robotic finger equipped with a tactile sensor and flexible tissue. Wellman and Howe⁴⁷ investigated the use of tactile sensors for the segmentation and detection of nodules embedded in tissue. Egorov and Sarvazyan¹⁵ proposed the use of tactile imaging for cancer detection and three-dimensional reconstruction of contrasting tissue. Miller *et al.*³³ developed capacitive array sensors for detecting small pulmonary nodules during video-assisted thoracoscopic surgery. Kaneko *et al.*²⁴ used stroboscopic imaging of pneumatically excited tissue for the same application. More recently, Liu *et al.*³⁰ and Althoefer *et al.*⁵ used various instrumented rolling

mechanical probes for measuring the normal stiffness of tissue and for segmentation of underlying hard nodules. Application of these works may be prohibited during MIS in deep surgical fields due to mechanical space constraints and additional time required for introduction of specialized instrumentation.

Estimation of mechanical impedance parameters of unknown environments dovetails with palpation schemes to provide a method for developing digital models of environments with varying stiffness properties. Love and Book³² presented a recursive least-squares algorithm for estimating one-dimensional environmental impedance parameters based on force data.* Kikuuwe and Yoshikawa²⁷ extended the impedance estimation methods to allow three-dimensional tensor estimates and segmentation of contact events. Erickson *et al.*¹⁶ presented an offline signal processing algorithm and compared it to three online methods for estimation of decoupled impedance parameters. Yamamoto *et al.*⁴⁹ compared impedance estimation algorithms in the context of teleoperated and autonomous one-dimensional impedance probing.

Significant progress was made by all these works; however, three major limitations remain unaddressed in applying shape, impedance, and contact estimation in the context of MIS. First, due to size constraints, minimally invasive surgical techniques in deep surgical sites including single port access surgery (SPAS)³ and natural orifice transluminal endoscopic surgery (NOTES)^{23,38} significantly limit the use of extraneous hardware such as tactile sensors, rolling elements, ultrasound probes, and other specialized modalities. Second, previous work did not investigate methods for automated shape and impedance exploration in unknown flexible environments. Third, previous work is limited to surface exploration and no attempts were made to identify constraints applied on a tool embedded in flexible media.

2.2. Research approach and contribution

The aforementioned limitations stem from serious technological and algorithmic challenges. We choose to overcome the first challenge of mechanical bulk and limited instrumentation by using force sensing data originating directly from the intracavitary robot end effectors. Robotic systems for minimally invasive surgery in deep surgical sites rely on deployable structures possessing local dexterity which is decoupled from gross motions at the insertion point into a body cavity or orifice. Integrated wrench sensing capability in surgical slaves has been an area of active research in the medical robotics community. Seibold *et al.*⁴⁰ describe a dedicated force-torque sensor at the end effector of a surgical instrument based on a Stewart-Gough platform with flexure hinges. Tavakoli *et al.*⁴³, Tholey and Desai⁴⁵, Trejos *et al.*⁴⁶ proposed wrench sensing on manual or remotely operated minimally invasive instrumentation with incorporated strain gauges mounted along the inserted length. Xu and Simaan⁴⁸ demonstrated wrench estimation

for surgical continuum robotics through intrinsic actuation force measurements. The proposed algorithms rely on force sensing at, or in close proximity to, the operation point of the robotic end effector. Thus, the algorithms, by design, do not require estimation of the effects of force reactions at the insertion point of the robotic system into the body cavity or at points displaced from the immediate surgical field.

Flexible media present a difficult challenge unmet by current exploration algorithms for robotic systems. The second limitation of estimating the shape and stiffness of flexible environments stems from the contradictory demands of the shape and stiffness estimation tasks. While accurate shape estimation in flexible environments requires minimal forces of interaction, precise stiffness estimation requires a certain level of force interaction to ensure a good signal to noise ratio. The third limitation of estimating constraints applied to a tool embedded in a flexible media stems from the difficulty in estimating the spatial stiffness matrix as opposed to estimating components of stiffness as is typically done in works focused on mechanical probing or stiffness imaging. These challenges were met by designing algorithms for first estimating the shape and subsequently estimating the impedance of the environment. The algorithms for estimating shape and stiffness require a balance between accuracy, time to scan completion, and memory requirements. We therefore devised a method for recursively adapting the scan resolution in a manner that is driven by the local neighborhood of explored stiffness matrices. The use of stiffness matrices provides geometric understanding that is not present in alternate techniques such as mechanical probing in a given direction or rolling contact stiffness imaging. We use this information by investigating the singular value decomposition of the local stiffness matrices and inferring directions of least and maximal resistance in order to guide movement of a deeply embedded surgical tool inside flexible anisotropic tissue.

The contribution of this paper is in presenting algorithms that expand autonomous robotic exploration procedures toward application in flexible, unstructured environments, such as an MIS operating field, with minimal sensing hardware requirements. Our approach utilizes surgical instruments with integrated wrench sensing capabilities as an exploration probe for characterizing both the shape and stiffness of an organ without the need for additional specialized sensors. The algorithms presented herein allow autonomous exploration and characterization of shape and mechanical impedance of intraoperative viscera while taking into account deep feature exploration in scenarios where the surgical tool is embedded inside a cleft within flexible tissue. A staged exploration is presented utilizing a hybrid force-motion control structure for shape exploration and a recursive estimation algorithm for mechanical impedance. A recursive algorithm for multi-resolution surface exploration is proposed based on local impedance estimates and stiffness contrasts. Finally, an algorithm for autonomous exploration of compliant anatomic features through stiffness segmentation is proposed. The algorithms presented constitute essential tools for enabling smart surgical devices capable of automated exploration and intraoperative modification of surgical plans.

* We refer to one-dimensional stiffness or impedance estimation as extraction of one component of a stiffness or impedance tensor in a specified direction.

3. Modeling Assumptions and Problem Statement

As described above, the proposed algorithms rely on force sensing at, or in close proximity to, the operation point of the robotic end effector. It is assumed that the surgical slave has an integrated wrench sensing capability. The algorithm evaluation uses an experimental platform with a six degree of freedom force/moment sensor as a means for development and evaluation of new algorithms for shape, stiffness, and constraint exploration within flexible environments.

Throughout our work, it is assumed that a human operator, e.g., the surgeon directing the procedure, defines an area of exploration analogous to an area of the MIS operating site. The robot controller then autonomously performs a staged exploration process. The mechanical properties of the explored medium are modeled as linear. While this assumption is incorrect for large deflections of tissue, for small deflections of the tissue (on the order of less than 1 mm), the assumption of local linearization is a reasonable simplification. This linear representation provides a first-order approximation of the time-varying, nonlinear characteristics of biologic tissue.¹⁹ The result is sufficient for creating a real-time model useful for identification of impedance contrast in the exploration region. Areas of rapidly changing stiffness can then be pursued further by definitive clinical metrics for diagnosis, such as biopsy, or for online control as demonstrated below. Further, the goal of our work is not to obtain a calibrated mechanical imaging modality, but to demonstrate methods that guide the exploration of shape while discovering features with different perceived impedance using stiffness contrasts. Finally, it is assumed throughout the work that the interaction of the exploration does not cause significant gross motion of the explored media. In the context of minimally invasive surgery, this assumption is practically implemented without additional tooling or control methods for abdominal viscera that are well supported by connective tissue and perivisceral fat such as the liver, spleen, and kidneys. For mobilized structures such as blood vessels, bowels, and stomach, a bimanual approach may be implemented to support the tissue while exploring. This is similar to the routine methods of tissue stabilization implemented during suturing and dissection.

We address the following problems in this investigation:

Problem 1. *Shape exploration and estimation in an unknown flexible environment.* Given a target exploration surface defined by the area, $A_E = \{([x_{min}, x_{max}], [y_{min}, y_{max}])\}$, define an exploration algorithm to safely explore and estimate the shape of a flexible environment.

Problem 2. *Impedance exploration for surface stiffness contrasts.* For the given exploration area, A_E , define an algorithm for estimating the three dimensional impedance parameters of the flexible environment and an adaptive exploration algorithm for estimating the mechanical impedance over the given area.

Problem 3. *Exploration of deep features.* Given a tool embedded in a fissure or a cleft within a flexible medium, define a method to guide exploration along the natural boundaries.

4. Algorithms for Exploration and Estimation

4.1. Nomenclature

The nomenclature used throughout the text is provided in Table 1 with a brief description. Further details are specified in the text where necessary.

4.2. Problem 1: Shape exploration and estimation

The shape exploration algorithm provides surface geometry estimate of the defined exploration region. The algorithm proposed herein performs a “blind” exploration, which can expand and augment a vision-based surface model. The robot end effector (EE) is tracked along the exploration surface using a hybrid force-motion control structure with inverse dynamics compensation, shown in Fig. 1, motivated by the work of Khatib²⁶ and Featherstone *et al.*¹⁷

The control structure requires decomposing desired motion and force trajectories into wrenches and twists that correspond to the constraint type using the projection matrices

$$\begin{aligned}\Omega &= \mathbf{N}(\mathbf{N}^T\mathbf{N})^{-1}\mathbf{N}^T = \mathbf{I} - \bar{\Omega}, \\ \bar{\Omega} &= \mathbf{T}(\mathbf{T}^T\mathbf{T})^{-1}\mathbf{T}^T = \mathbf{I} - \Omega,\end{aligned}\quad (1)$$

where \mathbf{N} is a $6 \times r$ matrix of linearly independent constraint wrench screws, r is the number of linearly independent constraints, and \mathbf{T} is a $6 \times (6 - r)$ matrix of linearly independent twist screws. The columns of the constraint wrench screws, \mathbf{N} , are given in ray line coordinates with force preceding moment, while the columns of the appropriate twists, \mathbf{T} , are expressed in axial line coordinates with linear velocity preceding angular velocity.³⁷

For surface scanning operations in a rigid environment, the space of controlled wrenches can be determined based on the estimation algorithms for the normal direction (e.g., Fedele *et al.*¹⁸, Yoshikawa and Sudou⁵⁰). Let unit vectors $\hat{\mathbf{u}}$, $\hat{\mathbf{v}}$, $\hat{\mathbf{w}}$ represent, respectively, the orthogonal directions in a coordinate frame defined with the $\hat{\mathbf{w}}$ -axis lying along the local normal to the surface. Matrices \mathbf{N} and \mathbf{T} are then given by the orthogonal directions of the local tangent frame

$$\mathbf{N} = \begin{bmatrix} \hat{\mathbf{w}} \\ \mathbf{0} \end{bmatrix}, \quad \mathbf{T} = \begin{bmatrix} \hat{\mathbf{u}} & \hat{\mathbf{v}} & \mathbf{0} & \mathbf{0} & \mathbf{0} \\ \mathbf{0} & \mathbf{0} & \hat{\mathbf{u}} & \hat{\mathbf{v}} & \hat{\mathbf{w}} \end{bmatrix}. \quad (2)$$

In contrast to rigid environments, shape exploration in compliant environments suffers a fundamental tradeoff between accuracy of the surface normal and surface position estimates. To best approximate the surface position, the surface deflection must be minimized. Hence, the interaction force between the robot and surface ideally must be minimized. Conversely, in order to estimate the local surface normal using the sensed force, the interaction force with the surface must be large enough to overcome signal-to-noise limitations of the force sensor and must therefore deform the surface.

In order to compensate for this trade-off during shape estimation with a hybrid controller requiring surface normal estimates, we use a simplified approach by specifying the direction of the controlled wrench as a constant in a local

Table I. Nomenclature for the exploration and estimation algorithms.

Symbol	Dimension	Description
r	Scalar	Number of linearly independent constraints at the operation point of a robotic end effector
\mathbf{N}	$\mathbb{R}^{6 \times r}$	Matrix of linearly independent constraint screws
\mathbf{T}	$\mathbb{R}^{6 \times (6-r)}$	Matrix of linearly independent twist screws
$\mathbf{\Omega}$	$\mathbb{R}^{6 \times 6}$	Constraint projection matrix
$\mathbf{\bar{\Omega}}$	$\mathbb{R}^{6 \times 6}$	Motion projection matrix
$\hat{\mathbf{u}}, \hat{\mathbf{v}}, \hat{\mathbf{w}}$	\mathbb{R}^3	Unit basis vectors of an arbitrary coordinate frame
a, b, ϕ	Scalar	Parameters defining prolate cycloid motion
n	Scalar	Dimension of the unknown environment parameters
T	Scalar	Sample period
k	Scalar	Sample number
\mathbf{f}_k	\mathbb{R}^3	Force sensor measurement at time kT
\mathbf{p}_k	\mathbb{R}^3	Position of EE at time kT , $\mathbf{p}_k = [x_k \ y_k \ z_k]^T$
$\mathbf{K}, \mathbf{B}, \mathbf{M}$	$\mathbb{R}^{3 \times 3}$	Impedance matrices of the compliant environment: Stiffness \mathbf{K} , Damping \mathbf{B} , and Mass \mathbf{M} .
\mathbf{z}_k	\mathbb{R}^3	Force history vector at time kT , $\mathbf{z}_k = \mathbf{f}_k + 2\mathbf{f}_{k-1} + \mathbf{f}_{k-2}$
$\boldsymbol{\varphi}_k$	\mathbb{R}^9	Position history vector at time kT , $\boldsymbol{\varphi}_k = [\mathbf{p}_k^T \ \mathbf{p}_{k-1}^T \ \mathbf{p}_{k-2}^T]^T$
\mathbf{h}_k	$\mathbb{R}^{3 \times n}$	Augmented coefficient matrix for the recursive estimator at time kT
$\mathbf{x}, \hat{\mathbf{x}}_k$	\mathbb{R}^n	Model parameter vector: actual and estimate at time kT
\mathbf{v}_k	\mathbb{R}^3	Measurement noise at time kT
\mathbf{Z}_k	\mathbb{R}^{3k}	Stacked measured output at time kT , $\mathbf{Z}_k = [\mathbf{z}_1^T \ \mathbf{z}_2^T \ \dots \ \mathbf{z}_k^T]^T$
\mathbf{H}_k	$\mathbb{R}^{3k \times n}$	Input matrix at time kT , $\mathbf{H}_k = [\mathbf{h}_1^T \ \mathbf{h}_2^T \ \dots \ \mathbf{h}_k^T]^T$
\mathbf{V}_k	\mathbb{R}^{3k}	Stacked measured noise at time kT , $\mathbf{V}_k = [\mathbf{v}_1^T \ \mathbf{v}_2^T \ \dots \ \mathbf{v}_k^T]^T$
\mathbf{w}_k	$\mathbb{R}^{3 \times 3}$	A diagonal weight matrix given by the inverse of the covariance of the sensor noise.
\mathbf{W}_k	$\mathbb{R}^{3k \times 3k}$	A block diagonal weight matrix composed of the weight matrices for the discrete time steps $1 \dots k$. $\mathbf{W}_k = \text{diag}(\mathbf{w}_1 \ \mathbf{w}_2 \ \dots \ \mathbf{w}_k)$
V	Scalar	Volume of an estimated stiffness ellipsoid
σ_i	Scalar	i^{th} singular values of an arbitrary matrix
c_m	Scalar	Scaling constant for the volume of a stiffness ellipsoid
A_E	$\mathbb{R}^{2 \times 2}$	Maxima and minima of the target exploration area $A_E = \{([x_{min}, x_{max}], [y_{min}, y_{max}])\}$
$step_{min}, step_{max}$	Scalar	Minimum and maximum stepsize respectively for the kernel search algorithm
ϵ	Scalar	Threshold for recursion during the <i>kernel search algorithm</i>
μ_p, μ_c	Scalar	Scaling factors for the predictor motion and corrector motions of the deep feature exploration algorithm
ϵ_f	Scalar	Threshold for force error during the corrector phase of the deep feature exploration algorithm

frame perpendicular to a global *a priori* estimate of the average normal direction. This estimate can be provided by preoperative imaging, intraoperative visualization or operator estimation. While this allows stable control in the unknown flexible environment, the use of a constant direction limits the algorithm to exploration of specified surface areas with small curvature over the search space. Despite the limitations imposed by the the constant direction, the algorithm is demonstratively effective for exploring small surface areas of a surgical site such as a limited patch or lobe as will be shown in the experimental section.

When the tissue surface is scanned based on a global *a priori* surface normal estimate, the estimated surface position is affected by the error between the global and local surface normal. Noting the hybrid controller only controls forces in wrench space, as the exploration surface deviates from the

predefined normal, the EE impinges into or diverges from the surface due to the uncompensated force in the motion direction (Fig. 2). The capability of the controller to maintain the probe position at the surface while moving in the “uphill” direction is degraded by the increase in friction due to this uncompensated force. As a result, surface estimates occur below the actual surface during exploration in this direction. For movement in the “downhill” direction, the controller is sufficiently fast with respect to the intended exploration motion to maintain contact with the surface. This directional phenomenon leads to an asymmetry in the estimate of surface position.

To compensate for bias in the surface estimation stemming from the direction of movement, a prolate cycloid motion is super imposed onto the overall search path to add redundancy in the estimation data for multiple motion

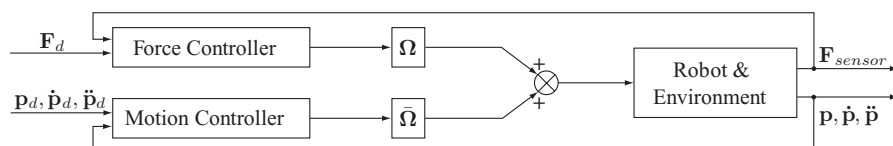


Fig. 1. Hybrid force-motion control architecture.

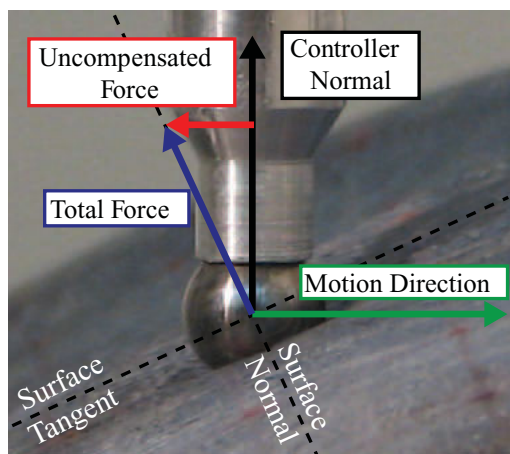


Fig. 2. (Colour online) Uncompensated force error in the motion space and corresponding deformation of a compliant material during the shape estimation.

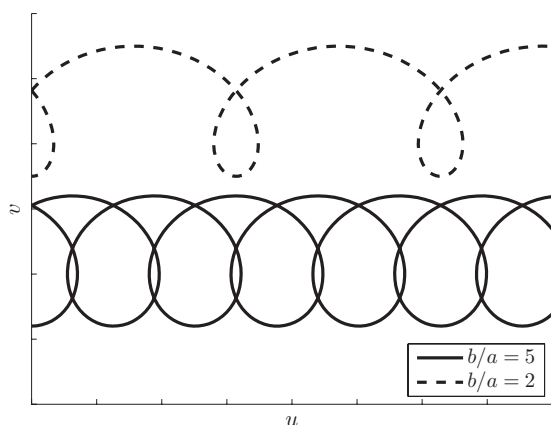


Fig. 3. Prolate cycloid motions in a local tangent plane. The solid and dashed paths represent different coverage based on the ratios of the trochoid parameters a and b .

directions, perpendicular to the surface normal estimate, at regular intervals. The additional local motion can be defined in the tangential motion space by the trochoid equations

$$u = a\phi - b \sin \phi, \quad v = a - b \cos \phi, \quad (3)$$

where u , v are the trochoid Cartesian coordinates as obtained by a tracer point offset by b units from the center of an imaginary circle with a radius of a units and rolling along the \hat{u} -axis. These parameters can be adjusted to control coverage overlap as depicted in Fig. 3.

The cycloid motion provides variance in the deformation of the flexible media and subsequent force in the motion space that allows intelligent use of a filter to better approximate the surface position. Though other scan patterns are possible and may result in better averaging of induced scan errors or filter parameters for the estimate, we evaluate this scan pattern, with respect to a straight line raster scan, due to ease of implementation and the overall scope of the presented work.

Data from this surface scan algorithm form a point cloud that can be used to fit a surface through interpolation techniques. The estimated surface can then be registered

to a larger surface such as three-dimensional vision surface reconstruction or intraoperative radiologic imaging data.

4.3. Problem 2: Impedance parameter exploration

Environment impedance estimates provide a method for modeling the interaction of the surgical slave with the operating environment for use in haptic models and define a method of anatomic segmentation based on contrasts in stiffness between neighboring tissue types, tissue planes, and pathologies. The impedance exploration algorithm produces an estimate of the mass, stiffness, and damping tensors of the robot EE interacting with the environment over the area previously explored for shape.

While the automatic shape exploration of the previous section is completed using continuous contact of the probe with the tissue, impedance parameter estimation of the tissue is carried out using digitized multi-resolution probing. During this process, the robot tip contacts the tissue at a given point and provides a local motion excitation in all directions while measuring the forces of interaction with the tissue. Once convergence of the impedance estimates is obtained, the robot tip leaves the tissue and moves to the next sampled point as determined by a high-level planning algorithm called the *kernel-search algorithm*.

The motivation for using digitized impedance point sampling is twofold. First, the tissue must be sampled and excited with respect to a start contact position where local tissue stresses are released. A continuous motion scan produces friction that pulls the tissue in the scan direction and corrupts impedance estimates. Second, the amount of data, computational resources, and memory required for continuous scan and impedance estimation are large and not justified considering the resolution required for planning and segmentation.

The kernel search algorithm provides a method for efficient multi-resolution impedance exploration. The algorithm searches the surface for features characterized by rapid stiffness change and adapts the scan resolution around these features to provide a better segmentation estimate while reducing the time required to estimate the impedance over an explored area. The algorithm requires *a priori* knowledge of the surface and boundaries to be specified by an operator or provided by the shape algorithm proposed in the previous section. The scan algorithm is further dependent on operator-defined parameters for the stiffness gradient threshold, ϵ , and the maximal and minimal discretization stepsizes, $step_{max}$ and $step_{min}$, respectively. A low-level algorithm that estimates the impedance parameters at discrete contact points within the compliant environment is first described. The kernel search algorithm is subsequently described in detail.

4.3.1. Local least-squares impedance estimation. To enable impedance estimation, we developed an algorithm based on Kikuuwe and Yoshikawa²⁷ and Ljung³¹ with the addition of a method for guaranteeing that the impedance parameters, namely the stiffness, damping, and mass matrices, are symmetric.

During surgical interaction, the position of the robot EE with respect to an equilibrium point and the force applied to

the environment are related as the following:

$$\mathbf{f}(t) = \mathbf{K}\mathbf{p}(t) + \mathbf{B}\dot{\mathbf{p}}(t) + \mathbf{M}\ddot{\mathbf{p}}(t). \quad (4)$$

The unknown local impedance tensors \mathbf{K} , \mathbf{B} , \mathbf{M} can be estimated based on the time-varying input position and output force information from the interaction. The force and position data are obtained, respectively, from the force sensor and from the direct kinematics of the robot.

The Laplace transform is applied to Eq. (4) to convert it to the frequency domain

$$\mathcal{L}(\mathbf{f}(t)) = (\mathbf{K} + s\mathbf{B} + s^2\mathbf{M})\mathcal{L}(\mathbf{p}(t)). \quad (5)$$

Applying the bilinear transform to Eq. (5) results in its discrete frequency domain representation. Applying an inverse Z-transform produces its discrete time approximation

$$\mathbf{z}_k = \left[\mathbf{K} + \left(\frac{2}{T}\right)\mathbf{B} + \left(\frac{4}{T^2}\right)\mathbf{M}, 2\mathbf{K} - \left(\frac{8}{T^2}\right)\mathbf{M}, \mathbf{K} - \left(\frac{2}{T}\right)\mathbf{B} + \left(\frac{4}{T^2}\right)\mathbf{M} \right] \boldsymbol{\varphi}_k = \boldsymbol{\Theta}^T \boldsymbol{\varphi}_k. \quad (6)$$

The goal of the estimation algorithm is to identify the 9×3 matrix $\boldsymbol{\Theta}$ containing all of the independent parameters of \mathbf{K} , \mathbf{B} , \mathbf{M} . Equation (6) can be cast into a classic linear regression form using the Kronecker product operator as

$$\mathbf{z}_k = \boldsymbol{\psi}_k^T \boldsymbol{\theta}, \quad (7)$$

where $\boldsymbol{\theta} = \text{Vec}(\boldsymbol{\Theta}^T)$ and $\boldsymbol{\psi}_k = \boldsymbol{\varphi}_k \otimes \mathbf{I}_{3 \times 3}^\dagger$.

For a physically realizable system, the mass and stiffness matrices should be symmetric positive definite and, assuming a symmetric form for the damping matrix, each of the impedance tensors of system models of Eqs. (4) through (7) contains three redundant parameters. This corresponds to redundant rows in $\boldsymbol{\theta}$ as follows:

$$\boldsymbol{\theta}_{9n+2} = \boldsymbol{\theta}_{9n+4}, \quad \boldsymbol{\theta}_{9n+3} = \boldsymbol{\theta}_{9n+7}, \quad \boldsymbol{\theta}_{9n+6} = \boldsymbol{\theta}_{9n+8} \quad (8)$$

for $n = 0, 1, 2$, where the subscripted term $\boldsymbol{\theta}_i$ denotes the i th element of vector $\boldsymbol{\theta}$.

Noting this redundancy, the regression matrix $\boldsymbol{\theta}$ can be reparameterized into a 18×1 vector,

$$\hat{\mathbf{x}} = [\boldsymbol{\theta}_1, \boldsymbol{\theta}_2, \boldsymbol{\theta}_3, \boldsymbol{\theta}_5, \boldsymbol{\theta}_6, \boldsymbol{\theta}_9, \boldsymbol{\theta}_{10}, \boldsymbol{\theta}_{11}, \boldsymbol{\theta}_{12}, \boldsymbol{\theta}_{14}, \boldsymbol{\theta}_{15}, \boldsymbol{\theta}_{18}, \dots, \boldsymbol{\theta}_{19}, \boldsymbol{\theta}_{20}, \boldsymbol{\theta}_{21}, \boldsymbol{\theta}_{23}, \boldsymbol{\theta}_{24}, \boldsymbol{\theta}_{27}]^T. \quad (9)$$

Using the definition of $\hat{\mathbf{x}}$ and accounting for measurement noise \mathbf{v} , one casts Eq. (7) into a discrete time approximation

[†] Given an $m \times n$ matrix \mathbf{A} , $\text{Vec}(\mathbf{A})$ is an mn length column vector constructed by sequentially stacking all columns of \mathbf{A} . Given the previously defined matrix \mathbf{A} and a $p \times q$ matrix \mathbf{B} , the Kronecker product is then given by the $mp \times nq$ matrix

$$\mathbf{A} \otimes \mathbf{B} = \begin{bmatrix} a_{11}\mathbf{B} & \dots & a_{1n}\mathbf{B} \\ \vdots & \ddots & \vdots \\ a_{m1}\mathbf{B} & \dots & a_{mn}\mathbf{B} \end{bmatrix}, \text{Graham}^{20}.$$

for the i th time step

$$\mathbf{z}_i = \mathbf{h}_i \hat{\mathbf{x}} + \mathbf{v}_i, \quad (10)$$

where \mathbf{h}_i represents an augmented coefficient matrix given by

$$\mathbf{h}_i = \begin{bmatrix} \mathbf{p}_i^T & \mathbf{0}_{1 \times 3} & \mathbf{p}_{i-1}^T & \mathbf{0}_{1 \times 3} & \mathbf{p}_{i-2}^T & \mathbf{0}_{1 \times 3} \\ \boldsymbol{\alpha}_i & \boldsymbol{\beta}_i & \boldsymbol{\alpha}_{i-1} & \boldsymbol{\beta}_{i-1} & \boldsymbol{\alpha}_{i-2} & \boldsymbol{\beta}_{i-2} \\ \boldsymbol{\chi}_i & \boldsymbol{\gamma}_i & \boldsymbol{\chi}_{i-1} & \boldsymbol{\gamma}_{i-1} & \boldsymbol{\chi}_{i-2} & \boldsymbol{\gamma}_{i-2} \end{bmatrix}, \quad (11)$$

and $\mathbf{p}_i^T = [x_i \ y_i \ z_i]$, $\boldsymbol{\alpha}_i = [0 \ x_i \ 0]$, $\boldsymbol{\beta}_i = [y_i \ z_i \ 0]$, $\boldsymbol{\chi}_i = [0 \ 0 \ x_i]$, $\boldsymbol{\gamma}_i = [0 \ y_i \ z_i]$.

Given k measurements, where $k \gg n$, the individual time steps of the regressor form can be stacked into an over-constrained linear system of the form

$$\mathbf{Z}_k = \mathbf{H}_k \hat{\mathbf{x}} + \mathbf{V}_k. \quad (12)$$

When sufficient data exist, the weighted least-squares criterion for estimation of the regression parameters is given by

$$\arg \min_{\hat{\mathbf{x}}} (\mathbf{Z}_k - \mathbf{H}_k \hat{\mathbf{x}})^T \mathbf{W}_k (\mathbf{Z}_k - \mathbf{H}_k \hat{\mathbf{x}}), \quad (13)$$

where the weight matrix, \mathbf{W}_k , is block-diagonal with \mathbf{w}_i along its diagonal. The optimal solution is given by

$$\hat{\mathbf{x}}_k = \mathbf{P}_k \mathbf{H}_k^T \mathbf{W}_k \mathbf{Z}_k, \quad (14)$$

where $\mathbf{P}_k^{-1} = \mathbf{H}_k^T \mathbf{W}_k \mathbf{H}_k$. With new measurements, the parameter estimate can be incrementally improved using a recursive linear estimation algorithm as in Crassidis and Junkins⁹,

$$\begin{aligned} \hat{\mathbf{x}}_{k+1} &= \hat{\mathbf{x}}_k + \mathbf{L}_{k+1} (\mathbf{z}_{k+1} - \mathbf{h}_k \hat{\mathbf{x}}_k) \\ \mathbf{L}_{k+1} &= \mathbf{P}_k \mathbf{h}_{k+1}^T (\mathbf{h}_k \mathbf{P}_k \mathbf{h}_{k+1}^T + \mathbf{w}_k^{-1})^{-1} \\ \mathbf{P}_{k+1} &= \mathbf{P}_k - \mathbf{L}_{k+1} \mathbf{h}_{k+1} \mathbf{P}_k. \end{aligned} \quad (15)$$

Elements of the impedance matrices are obtained by linear combinations of $\hat{\mathbf{x}}_k$ (see Appendix B for details). For time step k , the estimates are given by

$$\begin{aligned} \hat{\mathbf{K}}_i &= \frac{1}{4} (\hat{\mathbf{x}}_i + \hat{\mathbf{x}}_{i+6} + \hat{\mathbf{x}}_{i+12}) \\ \hat{\mathbf{B}}_i &= \frac{1}{4} T (\hat{\mathbf{x}}_i - \hat{\mathbf{x}}_{i+12}) \\ \hat{\mathbf{M}}_i &= \frac{1}{16} T^2 (\hat{\mathbf{x}}_i - \hat{\mathbf{x}}_{i+6} + \hat{\mathbf{x}}_{i+12}), \end{aligned} \quad (16)$$

where the subscript i denotes the element of the model parameter vector and the symmetric impedance matrices

given by

$$\mathbf{K} = \begin{bmatrix} K_1 & & sym \\ K_2 & K_4 & \\ K_3 & K_5 & K_6 \end{bmatrix}, \mathbf{B} = \begin{bmatrix} B_1 & & sym \\ B_2 & B_4 & \\ B_3 & B_5 & B_6 \end{bmatrix},$$

$$\mathbf{M} = \begin{bmatrix} M_1 & & sym \\ M_2 & M_4 & \\ M_3 & M_5 & M_6 \end{bmatrix}. \quad (17)$$

With an estimation method defined for individual points in an exploration field, it is left to define a method for directing the spacial locations for point explorations.

4.3.2. High-level kernel search algorithm. The kernel search algorithm directs impedance exploration and focuses on regions of rapidly changing impedance. This algorithm is an adaption of depth-limited search strategies for uninformed search that limit the search to a given problem space. The approach is optimal for impedance exploration of a surface since individual estimates are limited by the accuracy of the local data and the extent, and resolution of the scan can therefore be specified to a useful range by the operator. The method, described by the pseudocode in algorithm 1, drives the overall estimation by defining discrete locations, termed *search nodes*, for impedance estimation based on local environment parameters.

The kernel search algorithm begins with an initial path of search nodes discretizing the area and adaptively increases the resolution in areas of interest. The exploration proceeds along the defined search path and at each subsequent node the impedance parameters are estimated, GET-IMPEDANCE-PARAMS in algorithm 1, using a local sinusoidal forcing function and the impedance estimation algorithm of the previous section. A scalar metric of the stiffness is calculated based on the volume of the locally estimated stiffness

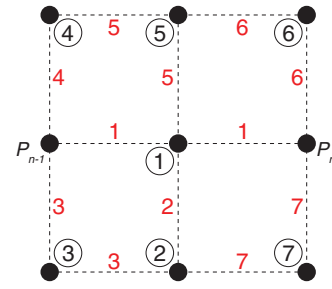


Fig. 4. (Colour online) Kernel Search Ordering. Node sequence is indicated by the encircled numbers. The sequence for comparing individual nodes (with respect to nodes palpated) given in uncircled numbers. Scan direction from P_{n-1} to P_n .

ellipsoid. The ellipsoid volume is proportional to the product of the singular values of the stiffness matrix

$$V = c_m \sigma_1 \sigma_2 \sigma_3. \quad (18)$$

Parameters σ_i ($i = 1, 2, 3$) denote the i th singular value of the local stiffness matrix \mathbf{K} . (See Nakamura³⁵ for details on singular value decomposition and ellipsoid volumes.) The constant c_m depends on the dimension of the stiffness matrix and, without loss of geometric information, is taken as $c_m = 1$ in Eq. (18).

As each new search node is explored and entered into the structure of explored nodes, the change in V is computed with respect to neighboring nodes. If this change exceeds a predefined threshold, the algorithm triggers a recursion to increase the density of nodes around the location of rapid stiffness change by constructing a new set of nodes, a *search kernel*, at a higher resolution and adapting the search path, ADD-KERNEL in algorithm 1.

Algorithm 1 Pseudocode for Kernel Search Algorithm

```

function KERNEL-SEARCH(searchParams) returns exploredNodes
  initialNodes ← GENERATE-INITIAL-NODES(searchParams)
  return RECURSIVE-KS(initialNodes, emptySet, stepmax, searchParams)
end function

function RECURSIVE-KS(queue, exploredNodes, stepSize, searchParams)
  returns exploredNodes
  for each Node in queue do
     $\mathbf{K}, \mathbf{B}, \mathbf{M}$  ← GET-IMPEDANCE-PARAMS(queue.current)
    exceedingPairs ← CHECK-THRESHOLDS(queue.current, exploredNodes, stepSize, searchParams)
    if stepSize > stepmin then
      for each Pair in exceedingPairs do
        newKernel ← ADD-KERNEL(Pair,  $\frac{stepSize}{2}$ , searchParams)
        exploredNodes ← RECURSIVE-KS(newKernel, exploredNodes,  $\frac{stepSize}{2}$ , searchParams)
      end for
    end if
  end for
  return exploredNodes
end function

```

searchParams holds the operator defined parameters of the kernel search: the search area A_E , the minimum and maximum stepsize $step_{min}$, $step_{max} = 2step_{min}$ for $i = 1, 2, \dots$, the threshold for recursion ϵ

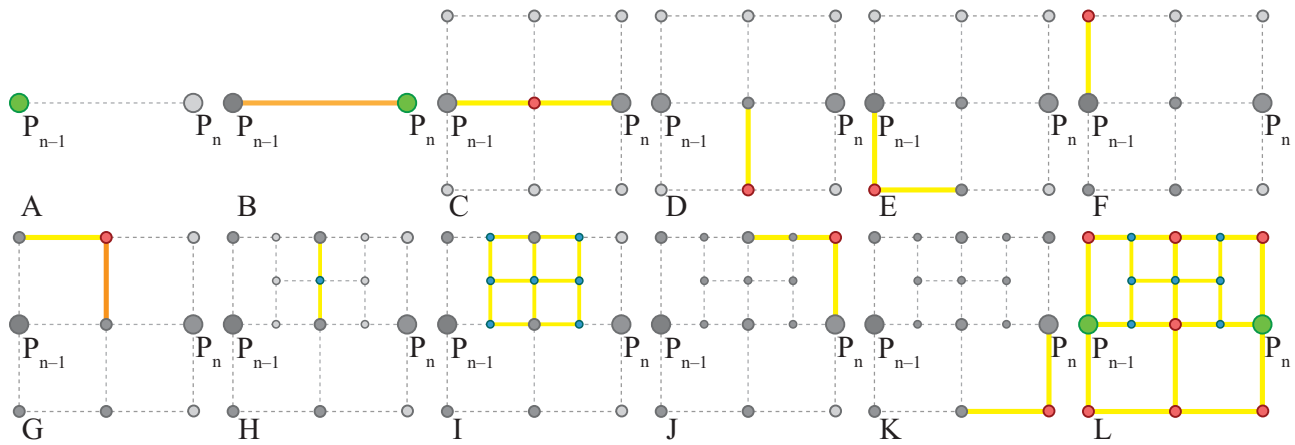


Fig. 5. (Colour online) Recursion search sequence in a local surface tangent space. (A) Palpating node P_{n-1} at the current resolution (1x). (B) Palpating node P_n at the current resolution. Threshold exceeded between points at P_{n-1} and P_n . (C) Kernel implemented at higher resolution (2x). First point in kernel palpated and neighboring function values compared. (D–F) Nodes in 2x resolution kernel palpated and neighboring function values compared. (G) Threshold exceeded between nodes. (H) Kernel implemented at higher resolution (4x). First point in kernel palpated. (I) Points in high resolution sequentially palpated and neighboring points compared. No differences above threshold discovered. Algorithm returns to 2x resolution. (J, K) Points in 2x resolution palpated with neighboring function values compared. (L) 2x kernel search complete, return to 1x resolution grid search, P_{n+1} .

The search kernel defines the geometric structure of nodes added to the overall grid of search locations in increasing levels of resolution. Figure 4 depicts the structure of the nodes in the added kernel and the sequence of exploration and comparison to ensure coverage at the increased resolution. The search kernel is implemented to adapt the current grid with an area of higher resolution by inserting the kernel at double the current resolution of the local nodes. Thus, the resolution increases by a factor of two in a small area surrounding the detected region of high stiffness contrast.

Search kernels are added to the overall plan recursively. Initially, a global discretization of the exploration area is generated based on a predefined maximal grid size. The initial scan path is generated by rasterizing this grid of nodes. The discretization and path generation functions are completed by GENERATE-INITIAL-NODES in algorithm 1. The exploration proceeds along this search path until the stiffness contrast threshold between explored nodes is exceeded, CHECK-THRESHOLDS in algorithm 1. With this detection, the search path is updated by the addition of a higher resolution set of search nodes in a last-in-first-out manner. The process of inserting kernels at higher resolution around areas of high contrast can continue recursively until the predefined highest resolution of the grid spacing, $step_{min}$, is reached.

The recursive queue of search nodes forces the exploration to return to the previous level of resolution and the algorithm proceeds until all initial nodes have been searched, thus ensuring coverage at the minimal resolution. The recursive sequence for increasing the scan resolution is depicted in Fig. 5.

The adaptive structure improves the efficiency of a discrete search over the exploration area. The constraints of exposure to the surgical site in MIS applications confine the total area of exploration to be small with respect to the robot size and speed. Thus, the time requirement for the exploration is predominantly characterized by the time to estimate the impedance parameters at a given location as opposed to

the time to move throughout the area and between points. Efficiency in the exploration is thereby improved by limiting the density of explored points to regions with large changes in the underlying impedance parameters.

A closed-form analytic expression for the time complexity of the kernel search algorithm is unavailable due to its adaptive structure. The upper and lower bounds of the search space are specified by the predefined maximum and minimum resolutions. To quantify the efficiency of applying the kernel search, the algorithm was tested empirically on a simulated exploration region using the Matlab[®] computing environment. A search area was generated with an underlying stiffness criterion function, Eq. (18), defined at each node such that the stiffness varied randomly from a constant value over the area. The random variations of all criterion values were drawn from a normal distribution with zero mean. Individual simulations with a given threshold for recursion, ϵ , and minimal stepsize, $step_{min}$, were run such that the simulated area was searched with a range of predefined search parameters. Results for a representative range of exploration parameters are presented in Fig. 6. The abscissa of the figure, R_g , is the ratio of discrete gradients, calculated between search nodes at the highest resolution, that exceeds the threshold, to the total number of node pairs. R_g thus serves as a metric for the variability of impedances in the search space relative to the threshold for recursion. The ordinate of the figure, R_s , is the ratio of nodes palpated to the total number of nodes at the highest resolution and thus serves as a metric for the time requirement of the search relative to an exhaustive search at the highest resolution.

The analysis displays both the advantages and limitations of the discrete sampling algorithm. As expected, the ratio of search nodes is bounded at the minimal resolution, $R_s \ll 1$, for search parameters with a low threshold for recursion and at the maximal resolution, $R_s = 1$, for a high threshold for recursion. The results suggest the algorithm allows for improvement in the time required for completion at the

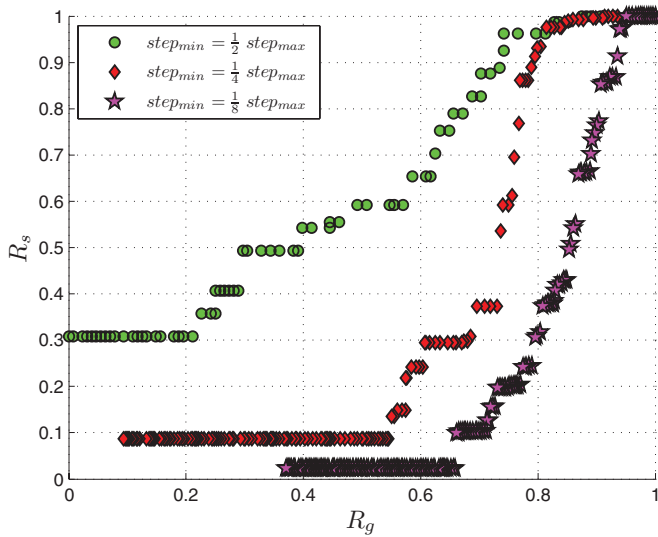


Fig. 6. (Colour online) Empirical evaluation of Kernel search algorithm efficiency. Abscissa: R_g , Ratio of discrete gradients above the threshold for recursion to the total of discrete gradients defined for the search area. Ordinate: R_s , Ratio of nodes palpated during exploration with the kernel search algorithm to number of nodes at the maximum resolution.

expense of possibly missing areas of interest with contrast below the threshold for recursion.

4.4. Problem 3: Exploration of deep features within a flexible environment

During surgery, instruments often interact with a cleft or fissure inside or between tissue features that define a natural three-dimensional anatomical constraint. Physical examples of application scenarios pertinent to MIS include exploring along dissection planes in a given tissue or between tissue types and through potential spaces such as tracking along the epicardial or pleural space. The premise behind the algorithm for deep feature exploration is that the geometry of the cleft and the tool are directly related to the perceived localized constraints applied by the tissue on a tool. A small local perturbation of the tool position and a judicious use of the impedance estimation algorithm result in a stiffness tensor that characterizes the local constraint applied by the tissue on the instrument.

Assume that a local exploration at point \mathbf{p} inside a cleft results in a stiffness matrix $\mathbf{K}(\mathbf{p})$. The stiffness ellipsoid

$$E_{\mathbf{K}} = \{ \Delta \mathbf{f} : \Delta \mathbf{f}^T \Delta \mathbf{f} = \Delta \mathbf{p}^T \mathbf{K}^T \mathbf{K} \Delta \mathbf{p} | \Delta \mathbf{p}^T \Delta \mathbf{p} = 1 \} \quad (19)$$

provides the perceived constraint forces for any pose perturbation within the unit deflections sphere $\Delta \mathbf{p}^T \Delta \mathbf{p} = 1$. The singular value decomposition $\mathbf{K} = \mathbf{U} \Sigma \mathbf{V}^T$ provides right singular vectors $\mathbf{V}^{[i]} = \Delta \hat{\mathbf{p}}_i^\dagger$, left singular vectors $\mathbf{U}^{[i]} = \Delta \hat{\mathbf{f}}_i$, and singular values σ_i , for $i = 1 \dots m$ such that $\mathbf{K} \Delta \hat{\mathbf{p}}_i = \sigma_i \Delta \hat{\mathbf{f}}_i$. Hence, the motion direction of least restraint, $\Delta \hat{\mathbf{p}}_{\min}$, corresponds to the direction $\mathbf{V}^{[i]}$ associated with the largest compliance (e.g., smallest singular value, σ_{\min} , of $\mathbf{K}(\mathbf{p})$).

Using this local information for $\Delta \hat{\mathbf{p}}_{\min}$, a predictor-corrector algorithm is defined for autonomous exploration of natural constraints. Pseudocode for the procedure is given in algorithm 2. The algorithm drives the robot a set distance, μ_p , along the predicted trajectory defined by $\Delta \hat{\mathbf{p}}_{\min}$ under force-monitored position control. Correction, to account for errors in the estimation of stiffness and to reduce local deformation in the tissue as a result of friction, is then applied by switching to admittance force control (see, for instance, Siciliano and Khatib⁴¹) allowing the position to be adjusted until the forces equilibrate or fall below a threshold ε_f . The algorithm repeats the cycle until a specified exploration distance is met or an end condition is satisfied.

5. Experimental Validation

To demonstrate the validity of the proposed algorithms, experiments were conducted to verify shape and impedance parameter estimates and to demonstrate exploration of deep features within tissue. To facilitate the interpretation of the results, visualizations of the surface estimation, and deep feature exploration are provided in multimedia extensions 1 and 2. (See Appendix A for instructions for online access and Table A1 for a description of the extensions.)

The experimental setup consisted of a system for simultaneous dynamic position control and force sensing as specified in the modeling assumptions, Section 3, and displayed in Fig. 7. A Cartesian robot was equipped with a

$\dagger \mathbf{A}^{[i]}$ represents the i th column of matrix \mathbf{A} .

Algorithm 2 Pseudocode for Deep Feature Exploration Algorithm

```

procedure DEEP-FEATURE-EXPLORE( $p_{start}$ ,  $completionCriteria$ )
   $\mathbf{p}_{current} \leftarrow \mathbf{p}_{start}$ 
  while false  $\leftarrow$  EXPLORATION-COMPLETE( $p_{start}$ ,  $completionCriteria$ ) do
     $\mathbf{K} \leftarrow$  PALPATE-POINT
     $\mathbf{U} \Sigma \mathbf{V}^T = \mathbf{K}$ 
     $\Delta \mathbf{p}_{min} \leftarrow \mathbf{V}^i : \arg \min \sigma_i$ 
     $\mathbf{p}_{current} \leftarrow \mathbf{p}_{current} + \mu_p \Delta \mathbf{p}_{min}$     comment: Predictor Step
    while  $\| \mathbf{f}_{sensor} \| > \varepsilon_f$  do
       $\mathbf{p}_{current} \leftarrow \mathbf{p}_{current} + \mu_c \frac{\mathbf{f}_{sensor}}{\| \mathbf{f}_{sensor} \|}$     comment: Corrector Step
    end while
  end while
end procedure

```

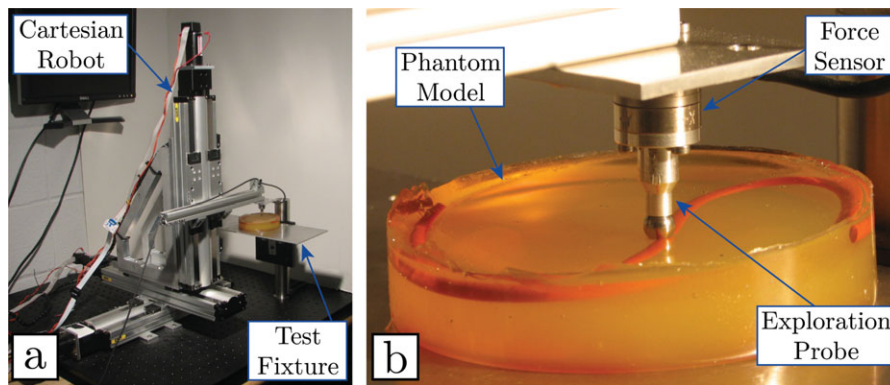


Fig. 7. (Colour online) (a) Overall experimental platform. (b) Force/torque sensor and probe interacting with an embedded feature phantom.

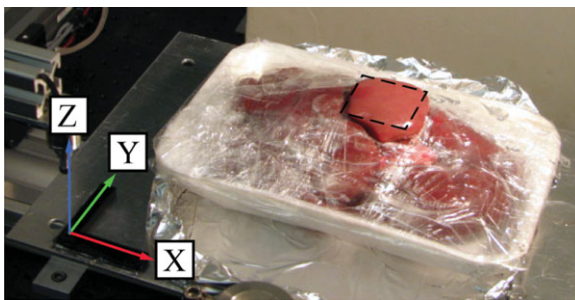


Fig. 8. (Colour online) Explanted bovine kidney tissue for shape estimation algorithm. Bounds for the shape estimation algorithm are highlighted.

Nano17 SI-25-0.25 6-axis force/torque sensor (ATI Industrial Automation, Apex, NC) and a 6.5 mm diameter spherical probe approximating the EE size of instruments common to the minimally invasive surgical environment. Centralized computed torque control (see Spong *et al.*⁴² for details) of the Cartesian robot was implemented in a real-time system running at 1 kHz. The force/torque signal was sampled at 5 kHz and a 40-point moving average filter was applied to reduce noise while minimizing phase shifts of the signal. The resolution of the force sensing obtained was 0.01 N after downsampling to the computed torque control frequency and applying an additional 30-point moving average filter. Table II summarizes the experimental conditions and results of the individual experiments demonstrating shape, impedance, and deep feature exploration. The details of the experimental conditions are provided explicitly in the following sections.

5.1. Shape estimation results

A bovine kidney was explored for validating the shape estimation algorithm. The tissue sample was fixed into the work volume of the Cartesian robot such that gross

rigid body motion of the kidney was effectively eliminated when subjected to the forces applied by the EE during the exploration experiment (less than 0.15 N) (Fig. 8). Throughout the experiment, the tissue was intermittently bathed in water to slow desiccation. Ground truth shape was measured manually using a portable coordinate measurement system (MicroScribe MLX, Immersion Corporation, San Jose CA). The coordinate measurement system has a dimensional accuracy of less than 0.13 mm though the surface measurement accuracy is limited by the ability of the operator to estimate probe contact.

An area of the surface was explored consecutively using, first, a prolate cycloid motion and, second, a straight raster scan to evaluate estimation accuracy with these scan approaches. The prolate cycloid scan parameters, Eq. (3), were defined as $a = \frac{1}{\pi}$ mm and $b = 2$ mm to augment a global raster pattern with a scan line spacing of 2 mm in a plane defined by the *a priori* surface normal used as the control input for the constraint wrench screw, Eq. 2. The mean error between the *a priori* estimate and the normals to the mesh of the ground truth data was 19° with a standard deviation of 8° and a maximum error of 38° . The scan parameters were chosen empirically to balance the time of exploration and exploration redundancy. The straight-line raster scan motion used identical alignment and raster line spacing. In both of the exploration tasks, the magnitude of the desired force of the hybrid controller (Fig. 1) was set slightly above the resolution of the force controller at 0.075 N.

During the exploration, the robot controller recorded the location of the EE at 1 kHz, and the data were used to generate a point cloud over the explored region. The cycloid scan data were subsequently filtered to remove points associated with force error in the motion space greater than a threshold of 0.02 N. The raster scan data showed limited force variation

Table II. Summary of experimental conditions.

Algorithm	Exploration media	Experimental results
Shape exploration	<i>Ex-vivo</i> bovine kidney tissue	Figs. 9, 10
Surface impedance exploration (Kernel search)	Inorganic rapid-prototyped phantom	Fig. 11
Deep feature exploration	Inorganic foam phantom, <i>ex-vivo</i> bovine kidney tissue	Figs. 12, 13

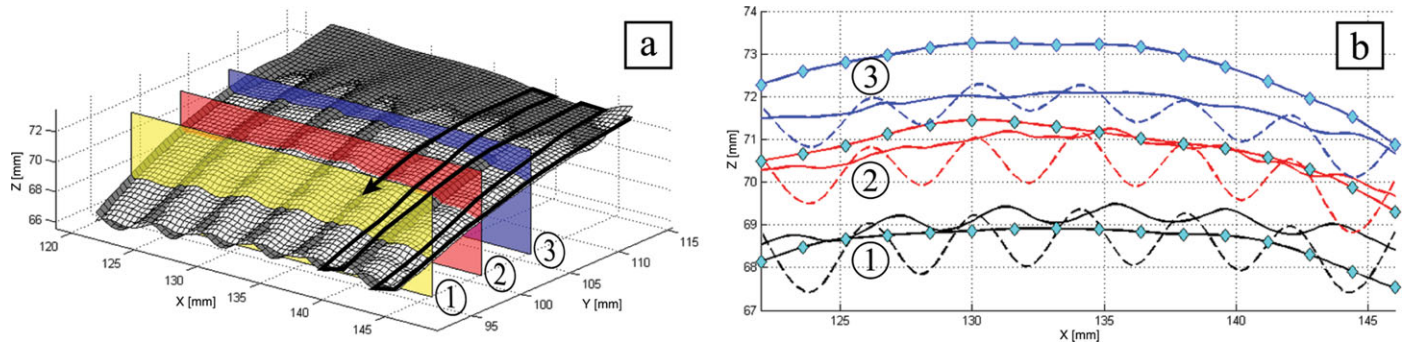


Fig. 9. (Colour online) Shape estimates for kidney lobe with hybrid force-motion controller. (a) Surface estimates using a prolate cycloid (white) and a straight-line raster scan (gray). The raster path is highlighted for a section of the scan. (b) Cross sections of the estimates at locations marked in (a) corresponding to $Y = 95, 100, 105$ mm with respect to the origin defined by the ground truth data. Solid line: cycloid scan estimate. Dashed line: straight raster scan estimate, Diamond-marked line: ground truth.

in the motion space during individual raster lines, hence the point data were not filtered using a threshold on the associated force measurements. The point cloud data for each scan was smoothed and a surface was generated in the Matlab[®] computing environment using the open source surface fitting algorithm “gridfit,” D’Errico¹², Fig. 9(a). The overall raster scan path is highlighted over a section of the surface by the heavy path line. Figure 9(b) presents cross sections of the estimated surface correlated with the section planes in Figure 9(a). Because the straight-line raster scan does not have a mechanism to compensate for bias due to the direction of motion, large oscillatory errors appear in the final estimated surface due to the biased local surface estimates between neighboring scan lines. In this investigation, the implementation of the cycloid motion allowed a 7.5% reduction in the maximum estimation error.

The error in the surface estimate as compared to the ground truth data is presented in Fig. 10. Results show a maximum estimation error in prediction of the surface to be less than ± 2.5 mm. These errors are comparable to existing clinically deployed computer-assisted navigation systems and robotic assistive systems using image-based registration techniques, Baert *et al.*⁸, Labadie *et al.*²⁸

5.2. Surface impedance estimation results

To validate the impedance exploration algorithm in a controlled environment with known stiffness features, a stiffness contrast phantom was manufactured by a multi-

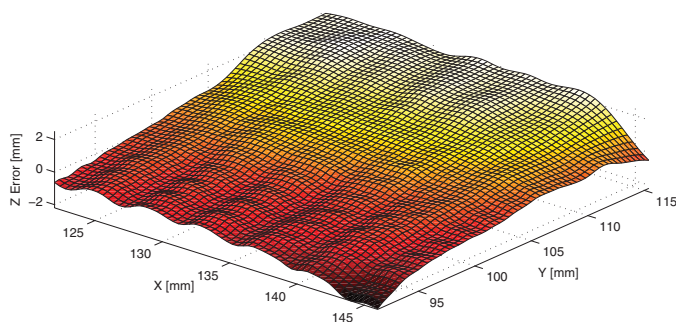


Fig. 10. (Colour online) Error in surface shape estimate for prolate cycloid scan.

material rapid prototyping process to yield nonrectilinear stiffness features. The process yielded a phantom of uniform thickness and hardness of Shore A 41 and Shore A 27, respectively, ASTM⁷, which could be supported in the test fixture of the experimental setup. A 16×16 mm area of the phantom was selected in order to cover both hard and soft sections. The surface impedance estimation algorithm of Section 4.3 was then run to test the success of autonomous stiffness exploration. The sinusoidal palpation parameters for the impedance estimation were specified with a peak-to-peak amplitude of 0.1 mm and a frequency of 0.8 Hz, 0.9 Hz, and 1.0 Hz, respectively, in the \hat{u} , \hat{v} , \hat{w} frames of the EE. The nonaligned frequencies were chosen to assure independence in the contributions to the force signal from motion in the orthogonal directions. The threshold for recursion was specified during the exploration at $\epsilon = 90 \text{ N/mm}^3$.

Results of the kernel search algorithm and the stiffness estimation algorithm show a clear differentiation of material stiffness normal to the material and minimal changes in the properties in the ellipsoids parallel to the exploration surface. Figure 11(a) displays the results of the estimate in the direction normal to the material. The algorithm successfully detected the spatially varying impedance and thus demonstrates a clear ability to differentiate stiffness contrast. Figure 11(b) shows planar cross sections of the stiffness ellipsoids together with their major and minor axes. The numbers by each ellipsoid designate the node order explored by the kernel search algorithm. The figure depicts the ability to adaptively increase the scan resolution when stiffness contrasts exceed the threshold for recursion. The kernel search algorithm limited the total search nodes to 85% of the total nodes at the maximum resolution and thus demonstrates the benefits for exploration effort and time saving.

An important limitation in estimating the impedance parameters occurs parallel to the surface. In this plane, the ellipsoid estimates were sensitive to the excitation parameters. This sensitivity can be attributed to two unmodeled factors in the environment interaction. As the robot EE moves with respect to the environment in the sinusoidal forcing function defined for the estimation algorithm, the contact area of the interaction varies and may be significantly different depending on the relative stiffness of

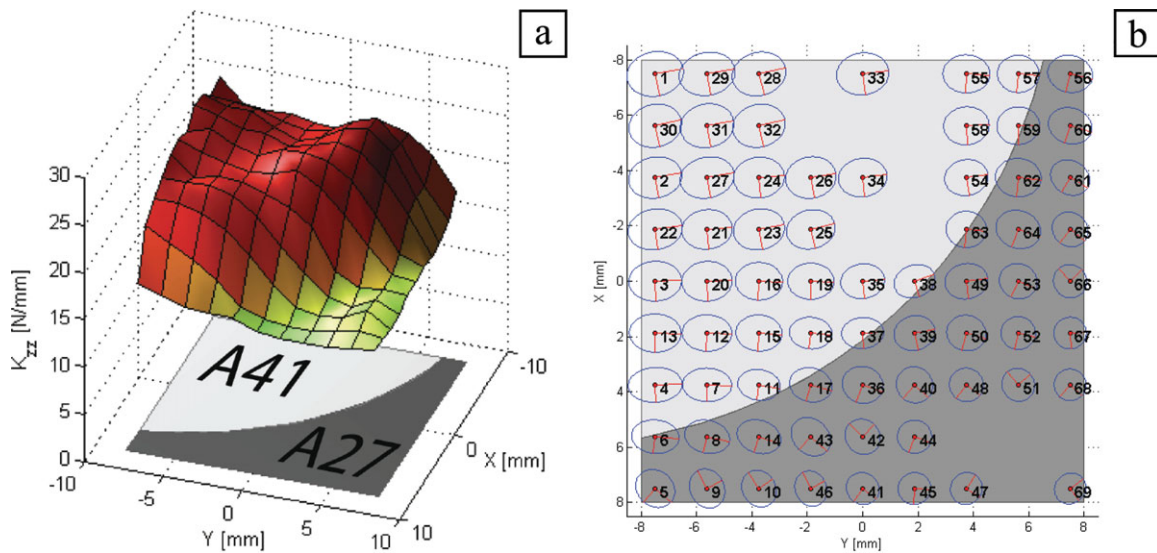


Fig. 11. (Colour online) Results of an impedance scan on an inorganic model. In both subfigures, the geometry of the underlying stiffness regions is denoted by the shaded regions. The light region corresponds to a region of Shore A41 and the dark region corresponds to Shore A27. (a) K_{zz} component of the stiffness tensor across the region of exploration. (b) Scan path and stiffness ellipsoids in plane of the explored surface. The search nodes are numbered by the order with which they were explored. The cross section of the stiffness ellipsoid in the plane at each explored node is displayed.

the environment and the threshold for interaction force with the tissue. Additionally, the tangential friction interaction is unmodeled in the EE-environment interaction, Eq. (4), and slip between the EE is assumed to be negligible. These effects are minimized by judicious choice of the excitation parameters of the low-level estimation algorithm in a way that minimizes environment deflections while ensuring a good signal to noise ratio for force measurements and minimizing the likelihood of tangential slip.

5.3. Deep feature exploration

Two experiments were carried out to evaluate the proposed algorithm for deep feature exploration. The first experiment used a foam phantom with an artificially-made sinusoidal cut. The second experiment used a bovine kidney with a naturally-occurring fissure. The inorganic material allows evaluation of the accuracy of our algorithm in guiding a probe to follow an artificial cut representing a cleft. This media

provides a controlled environment in which the accuracy of our proposed algorithms can be quantitatively evaluated without significant contamination of results by errors in estimation of the ground truth shape of a cleft in real tissue. The experiment on bovine kidneys as shown in Section 8 qualitatively validates the success of our algorithm on explanted tissue. As in the previous section, the sinusoidal palpation parameters were specified with a peak-to-peak amplitude of 0.1 mm and a frequency of 0.8 Hz, 0.9 Hz, and 1.0 Hz, respectively, in the \hat{u} , \hat{v} , \hat{w} frames of the EE.

5.3.1. Exploration in an inorganic phantom. A phantom material of packing foam with hardness suitable for containing computers and eliminating vibration was selected due to a qualitative similarity to tissue stiffness. The uncompressed density of the foam was 28.3 kg/m^3 . Given a 1 mm step indentation of the probe, the foam exhibited nonlinear stress relaxation with peak force of 0.22 N relaxing

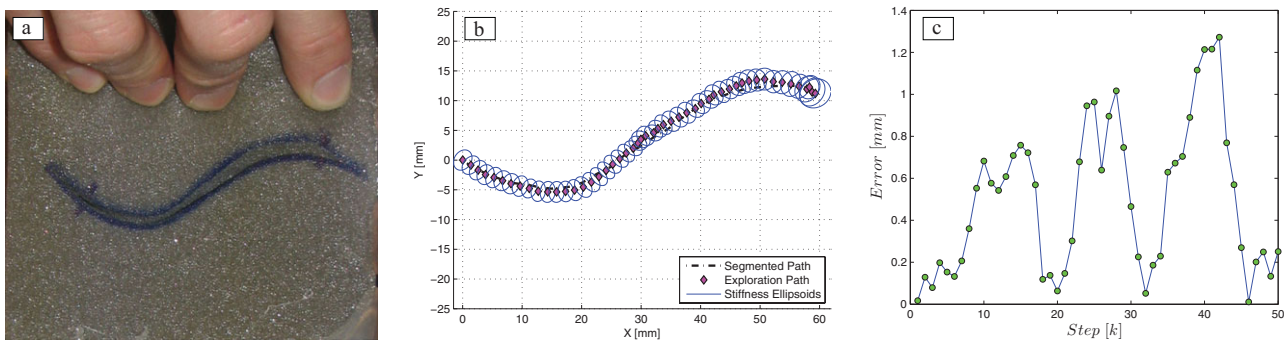


Fig. 12. (Colour online) Results of deep feature exploration in an inorganic phantom. (a) Exploration feature in foam phantom. The material is pulled away on one side to show the seam. (b) Exploration path and the estimated stiffness ellipsoids during exploration in the foam phantom model. (c) Results of deep feature exploration in an inorganic phantom.

to an equilibrium force of 0.15N with a time constant of 0.5 s. A sinusoidal seam was cut into the material as shown in Fig. 12(a). In the figure, the material is pulled away from one side to demonstrate the edge. This figure was also used for offline segmentation of the feature for comparison to the path explored by the robot.

The EE of the robot was inserted into the seam under force-monitored position control by a master command, similar to a surgeon initializing a robot to a given start position, (p_{start} in algorithm 2). The exploration algorithm then guided the robot autonomously along the length of the seam. For this demonstration, the motion of the EE was constrained to be parallel to the surface of the foam phantom. The stiffness ellipsoid estimates and the manually-segmented seam prescribing the ideal path in the plane of motion are displayed in Fig. 12(b). The experiment clearly demonstrates the efficacy of using the stiffness estimates for path planning. The error in the robot exploration path with respect to the segmented seam, Fig. 12(c), was less than 1.5 mm for all exploration points along the feature. Noting the force sensor used in the experimental apparatus was not optimal for the low force requirements of MIS, improvement in the sensitivity range, as demonstrated by the surgical instrumentation with integrated force sensing, will allow further improvement of the accuracy of exploration.

5.3.2. Exploration in ex-vivo bovine kidney. Analogous to the experiment with an inorganic material, the EE was positioned at a start point under master control at the beginning of a naturally-occurring seam in the tissue. The algorithm then guided the robot to autonomously explore the seam. Because the tissue had local hysteresis and was visually modified by the interaction, a representative ideal path could not be segmented. A representation of the EE at three points along the overall path is displayed in Fig. 13 with an overlay showing the stiffness ellipsoids for the entire exploration. Each ellipsoid shows the estimate of the local constraint in the plane of motion. The direction of the least resistance of the constraint is estimated as the minor axis of the stiffness ellipsoid.

The environment-EE interaction was critical to the performance in both the kidney and the inorganic foam experiments. The algorithm was developed under the assumption that the geometry of contact with the seam affects the perceived stiffness ellipsoid and the corrector step ensures that environment strain is minimized after the predictor step. The algorithm relies upon the relative lubricity of the media with respect to the robot EE and could lead to scenarios in which the algorithm cycles in place. If the predictor step moves the probe along the seam, but the probe does not slip with respect to the tissue, the corrector step may return the probe to the same position as the previous cycle, thus inhibiting exploration motion along the feature. The influence of lubricity can be visualized in Fig. 13 for $x = 8 - 10$ mm as apparent by the closely packed ellipsoids corresponding to large motions during the corrector step relative to sections of the path where friction was minimal. A possible solution to this problem would be increasing the prediction movement stepsize to break the friction with the tissue when cycling occurs during an exploration process.

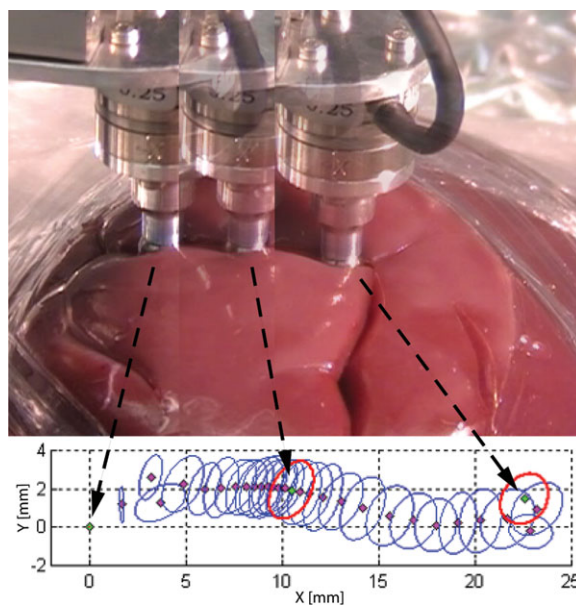


Fig. 13. (Colour online) Overlay of the exploration procedure at search nodes along the path defined by the anatomy. The upper overlay depicts the robot EE at three locations along an exploration path. The lower plot specifies the estimated stiffness ellipsoids in the plane of exploration along the search path. Ellipsoids corresponding to the instances in the upper photo are highlighted.

The overall experimental results demonstrate success of the algorithm for exploration in a highly unstructured environment. Singular value decomposition provides a clear methodology for estimating directions of minimal resistance to motion. The application of these local cues is sufficient for guiding exploration in naturally occurring anatomic constraints and, we believe, may be used for constructing local assistive telemanipulation virtual fixtures to aid surgeons in tasks of dissection along sensitive anatomy.

6. Conclusions

Three main challenges have been described in applying shape, impedance, and contact estimation in the context of minimally invasive surgery. These challenges include limitations in the size and specificity of instrumentation for deep site MIS, lack of frameworks for stiffness and shape exploration in flexible environments, and the lack of frameworks for constraint estimation during interaction of tools deeply embedded in flexible media. This paper makes a first step toward addressing these challenges by presenting a collection of algorithms that constitute an enabling technology for future generations of intelligent surgical robots to autonomously explore and acquire local environment properties of an MIS surgical sites.

The paper first presented a hybrid force-motion control algorithm for shape estimation and investigated the effects of the local scan pattern on the surface estimate. It was shown that a surface estimate based on data from a simplistic Cartesian raster scan pattern is corrupted as a result of frictional drag forces between the end effector probe and the flexible environment. A cycloid scan pattern was proposed with the aim of minimizing the effects of frictional drag forces on the surface estimate. Experiments showed

that the proposed cycloid scan significantly improves the surface estimate accuracy compared to Cartesian raster scan patterns.

As opposed to other approaches of unidirectional mechanical probing and stiffness imaging, this paper applied least-squares impedance estimation algorithms for inferring geometric data in order to guide exploration interaction environment interaction of surgical tools. An investigation into the structure of the least squares impedance estimation problem revealed a method for reducing the size of the data used during the recursive estimation process. Using this approach, a surgical tool can introduce a local perturbation to the tissue and obtain a local estimate of the impedance tensors.

Given the local estimates of impedance parameters, a high-level *kernel search* algorithm is presented as a means for autonomous surface exploration. This high-level algorithm guided the impedance parameter estimation of a surgical tool exploring the impedance of surface features. Experiments on a rapid-prototyped part with known geometry and stiffness demonstrated the utility of using tensor estimates of the impedance parameters for adapting the search space. It was shown that an appropriately set kernel search algorithm is a valid method for segmenting features with different stiffness within a flexible object.

The work finally presented a novel algorithm for exploring the shape of a cleft or fissure within an organ or along interconnecting tissue between adjacent organs. This algorithm for exploring deep features is based on a predictor-corrector strategy that utilizes local estimates of the stiffness tensor to guide the exploration motion. The algorithm was first evaluated on a foam specimen with an artificially generated cleft with a known geometry. The autonomous exploration successfully followed the geometry of the cleft with an accuracy of better than 1.5 mm. Subsequent validation on an explanted bovine kidney demonstrates the utility for autonomous exploration of an anatomical constraint.

We believe that the results and algorithms presented in this paper support the online acquisition of mechanical environment parameters and show the utility of mechanical *in-vivo* exploration of anatomy. Though the validation experiments successfully demonstrated the utility of our proposed algorithms, they also highlight limitations of our present work. An important limitation of the algorithms is the completion time for exploration that is only partially addressed by the adaptive search. To further improve on the execution and make these techniques applicable to time-critical applications, the investigated algorithms can be combined with continuous estimation techniques that provide fast gross information quickly and can then be expanded with discrete techniques. Combination of these algorithms will be the subject of future investigation.

References

1. J. J. Abbott and A. M. Okamura, "Stable forbidden-region virtual fixtures for bilateral telemanipulation," *J. Dyn. Syst. Meas. Control* **128**(1), 53–64 (2006).
2. S. Ahmad and C. N. Lee, "Shape recovery from robot contour-tracking with force feedback," *Adv. Robot.* **5**(3), 257–273 (Jan. 1990).
3. P. Allemann, M. Schafer and N. Demartines, "Critical appraisal of single port access cholecystectomy," *Br. J. Surg.* **97**(10), 1476–1480 (Jul. 2010).
4. P. Allen and P. Michelman, "Acquisition and interpretation of 3-D sensor data from touch," *IEEE Trans. Robot. Autom.* **6**(4), 397–404 (1990).
5. K. Althoefer, D. Zbyszewski, H. Liu, P. Puangmali, L. Seneviratne, B. Challacombe, P. Dasgupt and D. Murphy, "Air-cushion force sensitive probe for soft tissue investigation during minimally invasive surgery," **In: Sensors**, 2008 IEEE. Lecce, Italy (2008) pp. 827–830.
6. R. Araujo, U. Nunes, A. T. de Almeida, "3D surface-tracking with a robot manipulator," *J. Intell. Robot. Syst.* **15**(4), 401–417 (Apr. 1996).
7. ASTM, D2240-00 Standard Test Method for Rubber Property - Durometer Hardness (2000).
8. A. L. Baert, M. Knauth, K. Sartor, E. Neri, D. Caramella, C. Bartolozzi, J. Kettenbach, G. Kronreif, A. Melzer, G. Fichtinger, D. Stoianovici and K. Cleary, "Ultrasound-, CT- and MR-Guided robot-assisted interventions," **In: Medical Radiology** (Springer Berlin Heidelberg, Berlin, Heidelberg, 2008) pp. 393–409.
9. J. L. Crassidis and J. L. Junkins, *Optimal Estimation of Dynamic Systems* (CRC Press, Boca Raton, FL 2004).
10. P. Dario, B. Hannaford and A. Menciassi, "Smart surgical tools and augmenting devices," *IEEE Trans. Robot.* **19**(5), 782–792 (2003).
11. T. J. Debus, P. E. Dupont and R. D. Howe, "Contact state estimation using multiple model estimation and hidden Markov models," *Int. J. Robot. Res.* **23**(4), 399–413 (Apr. 2004).
12. J. D'Errico. Surface Fitting using gridfit, MATLAB Central File Exchange. Retrieved April 13, 2009.
13. Z. Dougeri and Y. Karayiannidis, "Force/position regulation for a robot in compliant contact using adaptive surface slope identification," *IEEE Trans. Autom. Control* **53**(9), 2116–2122 (Oct. 2008).
14. B. Eberman, "A model-based approach to cartesian manipulation contact sensing," *Int. J. Robot. Res.* **16**(4), 508–528 (Aug. 1997).
15. V. Egorov and A. P. Sarvazyan, "Mechanical imaging of the breast," *IEEE Trans. Med. Imaging* **27**(9), 1275–1287 (2008).
16. D. Erickson, M. Weber and I. Sharf, "Contact stiffness and damping estimation for robotic systems," *Int. J. Robot. Res.* **22**(1), 41–57 (2003).
17. R. Featherstone, S. S. Thiebaut and O. Khatib, "A General Contact Model for Dynamically-Decoupled Force/Motion Control," **In: Proceedings of the 1999 IEEE International Conference on Robotics and Automation**, Detroit, Michigan (1999) pp. 3281–3286.
18. A. Fedele, A. Fioretti, C. Manes and G. Ulivi, "On-Line Processing of Position and Force Measures for Contour Identification and Robot Control," **In: Proceedings of the 1993 IEEE International Conference on Robotics and Automation**, Atlanta, GA (1993) pp. 369–374.
19. Y. C. Fung, *Biomechanics: Mechanical Properties of Living Tissues*, 2nd ed. (Springer-Verlag, New York, 1993).
20. A. Graham, *Kronecker Products and Matrix Calculus: With Applications* (Halsted Press, New York, 1981).
21. S. C. Ho, R. D. Hibberd and B. L. Davies, "Robot assisted knee surgery," *IEEE Eng. Med. Biol.* **14**(May/June), 292–299 (1995).
22. S. Jung, T. Hsia and R. Bonitz, "Force tracking impedance control of robot manipulators under unknown environment," *IEEE Trans. Control Syst. Technol.* **12**(3), 474–483 (May 2004).
23. A. N. Kallou, V. K. Singh, S. B. Jagannath, H. Niiyama, S. L. Hill, C. A. Vaughn, C. A. Magee and S. V. Kantsevov, "Flexible transgastric peritoneoscopy: A novel approach to diagnostic and therapeutic interventions in the peritoneal cavity," *Gastrointestinal Endoscopy* **60**(1), 114–117 (2004).
24. M. Kaneko, C. Toya and M. Okajima, "Active Strobe Imager for Visualizing Dynamic Behavior of Tumors" **In: Proceedings**

- of the 2007 IEEE International Conference on Robotics and Automation, Rome, Italy (2007) pp. 3009–3014.
25. A. Kapoor, M. Li and R. H. Taylor, "Spatial Motion Constraints for Robot Assisted Suturing using Virtual Fixtures," Vol. LNCS 3750. Springer-Verlag, Palm Springs, CA (2005) pp. 89–96.
 26. O. Khatib, "A unified approach for motion and force control of robot manipulators: The operational space formulation," *IEEE Trans. Robot. Autom.* **RA-3**(1), 43–53 (1987).
 27. R. Kikuuwe and T. Yoshikawa, "Robot perception of environment impedance," *J. Robot. Syst.* **22**(5), 231–247 (2005).
 28. R. F. Labadie, B. M. Davis and J. M. Fitzpatrick, "Image-guided surgery: What is the accuracy?," *Curr. Opin. Otolaryngol. Head and Neck Surg.* **13**(1), 27–31 (Feb. 2005).
 29. T. Lefebvre, H. Bruyninckx, J. De Schutter, *Nonlinear Kalman Filtering for Force-Controlled Robot Tasks*. Vol. 19 (Springer, 2005).
 30. H. Liu, D. p. Noonan, B. J. Challacombe, P. Dasgupta, L. D. Seneviratne and K. Althoefer, "Rolling mechanical imaging for tissue abnormality localization during minimally invasive surgery," *IEEE Trans. Biomed. Eng.* **57**(2), 404–414 (2010).
 31. L. Ljung, *System Identification, Theory for the User*, 2nd ed. (Prentice Hall PTR, Upper Saddle River, 1999).
 32. L. J. Love and W. J. Book, "Environment Estimation for Enhanced Impedance Control," *Proc. 1995 IEEE Int. Conf. Robot. Autom.* **2**, 1854–1859 (1995).
 33. A. P. Miller, W. J. Peine, J. S. Son and Z. T. Hammoud, "Tactile Imaging System for Localizing Lung Nodules During Video Assisted Thoracoscopic Surgery," *In: Proceedings of the 2007 IEEE International Conference on Robotics and Automation* (2007) pp. 2996–3001.
 34. M. Moll and M. A. Erdmann, "Reconstructing Shape from Motion using Tactile Sensors," *In: Proceedings of the 2001 IEEE/RSJ International Conference on Intelligent Robots and Systems*. Vol. 2. Maui, HI, United States (2001) pp. 692–700.
 35. Y. Nakamura, *Advanced Robotics: redundancy and optimization* (Addison Wesley Publishing, Reading, 1991).
 36. A. M. Okamura and M. R. Cutkosky, "Feature Guided Exploration with a Robotic Finger," *In: Proceedings of the 2001 IEEE International Conference on Robotics and Automation* (2001) pp. 589–596.
 37. H. Pottmann and J. Wallner, *Computational Line Geometry* (Springer, 2001).
 38. W. O. Richards and D. W. Rattner, "Endoluminal and transluminal surgery: No longer if, but when," *Surg. Endoscopy* **19**(4), 461–463 (Apr. 2005).
 39. A. M. Sabatini, P. Dario and M. Bergamasco, "Interpretation of mechanical properties of soft tissues from tactile measurements," *Exp. Robotics* **139**, 152–162 (1990).
 40. U. Seibold, B. Kubler and G. Hirzinger, "Prototype of Instrument for Minimally Invasive Surgery with 6-Axis Force Sensing Capability," *In: Proceedings of the 2005 IEEE International Conference on Robotics and Automation* (2005) pp. 498–503.
 41. B. Siciliano and O. Khatib, *Springer Handbook of Robotics* (Springer-Verlag, Berlin, 2008).
 42. M. W. Spong, S. Hutchinson and M. Vidyasagar, *Robot Modeling and Control* (Wiley, Hoboken, NJ 2005).
 43. M. Tavakoli, R. Patel and M. Moallem, 2005. "Haptic interaction in robot-assisted endoscopic surgery: A sensorized end-effector," *Int. J. Med. Robot. Comput. Assist. Surg.* **01**(02), 53.
 44. R. Taylor and D. Stoianovici, "Medical robotics in computer-integrated surgery," *IEEE Trans. Robot. Autom.* **19**(5), 765–781 (2003).
 45. G. Tholey and J. P. Desai, "A compact and modular laparoscopic grasper with tridirectional force measurement capability," *J. Med. Devices* **2**(3), 031001(1–8) (2008).
 46. A. L. Trejos, R. V. Patel, M. D. Naish, A. C. Lyle and C. M. Schlachta, "A sensorized instrument for skills assessment and training in minimally invasive surgery," *J. Med. Devices* **3**(4), 041002 (2009).
 47. P. S. Wellman and R. D. Howe, "Extracting Features from Tactile Maps," *In: Proceedings of the Second International Conference on Medical Image Computing and Computer-Assisted Intervention* Volume 167 (1999) pp. 11–1142.
 48. K. Xu and N. Simaan, Jun. "Intrinsic wrench estimation and its performance index for multisegment continuum robots," *IEEE Trans. Robot.* **26**(3), 555–561 (2010).
 49. T. Yamamoto, M. Berhardt, A. Peer, M. Buss and A. M. Okamura, "Techniques for Environment Parameter Estimation During Telemanipulation," *In: Proceedings of the 2nd Biennial IEEE/RAS-EMBS International Conference on Biomedical Robotics and Biomechatronics* (2008) pp. 217–223.
 50. T. Yoshikawa and A. Sudou, "Dynamic hybrid position/force control of robot manipulators - on-line estimation of unknown constraint," *IEEE Trans. Robot. Autom.* **9**(2), 220–226 (1993).
 51. T. Yoshikawa, Y. Yu and M. Koike, "Estimation of Contact Position between Object and Environment Based on Probing of Robot Manipulator," *In: Proceedings of the 1996 IEEE/RSJ International Conference on Intelligent Robots and Systems '96, IROS 96*. Vol. 2 (1996) pp. 769–776.

Appendix A. Multimedia Extensions

Multimedia extensions can be accessed online at

<http://research.vuse.vanderbilt.edu/arma/Media/compliant-algorithms.shtml>

Table A1. Multimedia extensions with description of material.

Extension	Type	Description
1	Video	Demonstration of shape exploration with cycloid motion
2	Video	Demonstration of deep feature exploration

Appendix B. Impedance Tensor Elements from the Model Parameter Vector

Given a model parameter vector estimate, $\hat{\mathbf{x}}$, the impedance matrices can be reconstructed by algebraic manipulation of Eqs. (6)–(9). Noting the redundant parameters in the original parameter vector, $\boldsymbol{\theta} = \text{Vec}(\boldsymbol{\Theta}^T)$, given by (9), $\hat{\mathbf{x}}$ can be expanded to yield

$$\boldsymbol{\theta} = [\hat{\mathbf{x}}_1, \hat{\mathbf{x}}_2, \hat{\mathbf{x}}_3, \hat{\mathbf{x}}_2, \hat{\mathbf{x}}_4, \hat{\mathbf{x}}_5, \hat{\mathbf{x}}_3, \hat{\mathbf{x}}_5, \hat{\mathbf{x}}_6, \hat{\mathbf{x}}_7, \hat{\mathbf{x}}_8, \hat{\mathbf{x}}_9, \hat{\mathbf{x}}_8, \hat{\mathbf{x}}_{10}, \dots, \hat{\mathbf{x}}_{11}, \hat{\mathbf{x}}_9, \hat{\mathbf{x}}_{11}, \hat{\mathbf{x}}_{12}, \hat{\mathbf{x}}_{13}, \hat{\mathbf{x}}_{14}, \hat{\mathbf{x}}_{15}, \hat{\mathbf{x}}_{14}, \hat{\mathbf{x}}_{16}, \hat{\mathbf{x}}_{17}, \hat{\mathbf{x}}_{15}, \hat{\mathbf{x}}_{17}, \hat{\mathbf{x}}_{18}] \quad (\text{B1})$$

where the subscripted variable, $\hat{\mathbf{x}}_i$, denotes the i th element of the model parameter vector estimate, $\hat{\mathbf{x}}$. By reversing the vector operator, the matrix, $\boldsymbol{\Theta}$, can be reconstructed as

$$\boldsymbol{\Theta}^T = \begin{bmatrix} \hat{\mathbf{x}}_1 & \hat{\mathbf{x}}_2 & \hat{\mathbf{x}}_3 & \hat{\mathbf{x}}_7 & \hat{\mathbf{x}}_8 & \hat{\mathbf{x}}_9 & \hat{\mathbf{x}}_{13} & \hat{\mathbf{x}}_{14} & \hat{\mathbf{x}}_{15} \\ \hat{\mathbf{x}}_2 & \hat{\mathbf{x}}_4 & \hat{\mathbf{x}}_5 & \hat{\mathbf{x}}_8 & \hat{\mathbf{x}}_{10} & \hat{\mathbf{x}}_{11} & \hat{\mathbf{x}}_{14} & \hat{\mathbf{x}}_{16} & \hat{\mathbf{x}}_{17} \\ \hat{\mathbf{x}}_3 & \hat{\mathbf{x}}_5 & \hat{\mathbf{x}}_6 & \hat{\mathbf{x}}_9 & \hat{\mathbf{x}}_{11} & \hat{\mathbf{x}}_{12} & \hat{\mathbf{x}}_{15} & \hat{\mathbf{x}}_{17} & \hat{\mathbf{x}}_{18} \end{bmatrix} = [\mathbf{A}_1, \mathbf{A}_2, \mathbf{A}_3]. \quad (\text{B2})$$

Noting from (1), the matrix represents a linear combinations of the impedance parameters where

$$\begin{aligned} \mathbf{A}_1 &= \mathbf{K} + \frac{2}{T}\mathbf{B} + \frac{4}{T^2}\mathbf{M}, \quad \mathbf{A}_2 = 2\mathbf{K} - \frac{8}{T^2}\mathbf{M}, \\ \mathbf{A}_3 &= \mathbf{K} - \frac{2}{T}\mathbf{B} + \frac{4}{T^2}\mathbf{M}. \end{aligned} \quad (\text{B3})$$

It can be easily verified that

$$\begin{aligned} \mathbf{K} &= \frac{1}{4}(\mathbf{A}_1 + \mathbf{A}_2 + \mathbf{A}_3), \quad \mathbf{B} = \frac{T}{4}(\mathbf{A}_1 - \mathbf{A}_3), \\ \mathbf{M} &= \frac{T^2}{16}(\mathbf{A}_1 - \mathbf{A}_2 + \mathbf{A}_3). \end{aligned} \quad (\text{B4})$$